nuclear fusion

Impurity leakage mechanisms in the Wendelstein 7-X island divertor under friction-dominated conditions

To cite this article: V.R. Winters *et al* 2024 *Nucl. Fusion* **64** 056042

OPEN ACCESS
IOP Publishing | International Atomic Energy Agency
Nuclear Fusion
Nucl. Fusion **64** (2024) 056042 (12pp)
https://doi.org/10.1088/1741-4326/ad3768

Impurity leakage mechanisms in the Wendelstein 7-X island divertor under friction-dominated conditions

V.R. Winters*, F. Reimold, Y. Feng, V. Perseo, M. Beurskens, S. Bozhenkov, K.J. Brunner, G. Fuchert, R. Koenig, J. Knauer, M. Krychowiak, E. Pasch, E. Scott, D. Zhang and the W7-X Team[a]

Max-Planck-Institut für Plasmaphysik, 17491 Greifswald, Germany

E-mail: victoria.winters@ipp.mpg.de

Received 7 December 2023, revised 7 March 2024
Accepted for publication 25 March 2024
Published 18 April 2024

Abstract

The EMC3-Eirene code was used to study the main impurity leakage mechanism for the island divertor in the standard magnetic field configuration. It was found that under experimentally accessible plasma scenarios in the last experimental campaign, the majority of the island scrape-off layer was friction-force dominated. The impurity force balance was only thermal force dominated for upstream locations closed to the last closed flux surface, beyond the island X-point. No impurity neutral ionization was found in this location and hence the parallel impurity transport provides excellent impurity retention. It was found that impurities approach the confinement region nonetheless via perpendicular transport across the island O-point near the parallel flow stagnation region. This finding points out the specific role of the parallel flow stagnation region in providing lower parallel convective transport and long impurity residence times, which makes non-parallel transport channels more important or even the dominant driver of impurity leakage. In line with the relevance of the particle build-up in the flow stagnation region, different retention behavior as a function of density is seen for various species, which is shown to be due to ionization length changes as the plasma background density is increased.

Keywords: stellarator, impurity transport, scrape-off layer, EMC3-Eirene

(Some figures may appear in colour only in the online journal)

1. Introduction

The Wendelstein 7-X (W7-X) island divertor concept is currently being assessed for its possible relevance in a stellarator reactor. One critical aspect of this assessment is the island divertor's ability to retain and exhaust impurities, both from intrinsic as well as extrinsic sources. The retention of impurities can be quantified by parameters such as compression (the ratio of the divertor impurity density to the core impurity density, $n_{z,\mathrm{div}}/n_{z,\mathrm{core}}$) and enrichment (the ratio of the divertor impurity concentration to the core impurity concentration, $c_{z,\mathrm{div}}/c_{z,\mathrm{core}}$) [1, 2]. High impurity retention in the divertor achieves two important goals:

(i) For a given acceptable impurity content in the confined plasma, it allows for a greater density of impurities in the divertor and at the pumps, allowing for higher scrape-off layer (SOL) radiation losses and better impurity exhaust (critical for helium ash).

---

[a] See Grulke *et al* 2024 (https://doi.org/10.1088/1741-4326/ad2f4d) for the W7-X Team.

[*] Author to whom any correspondence should be addressed.

(ii) Larger retention also means that for a given impurity source there is less core contamination. This implies larger resilience against high Z intrinsic impurities, such as tungsten, where even small amounts would lead to unacceptable radiated losses in the core [3].

This work aims to elucidate the dominant physics mechanisms limiting the impurity retention in the W7-X operational spaces using EMC3-Eirene [4]. The simulation results allow us to isolate effects of perpendicular versus parallel transport and how this interplays with the impurity ionization location to cause changes in impurity leakage. Section 2 will discuss the physics background and simulation set-up. Section 3 will present the simulation results and their interpretation. Finally, section 4 will discuss the limitations of the simulation results, in particular the role of drifts, and will conclude.

2. Background and simulation set-up

2.1. W7-X island geometry

W7-X is a 5-fold symmetric, quasi-isodynamic stellarator [5]. Each of the 5 toroidal modules contains 2 divertor target plates: one on the upper and one on the lower half of the machine [6]. The targets intersect magnetic islands which form naturally on a rational surface at the plasma edge. The magnetic field configuration investigated in this work is the standard magnetic field configuration. The island SOL in the standard configuration consists of 5 independent magnetic islands formed at the 5/5 resonance. Each island intersects 2 of 10 total divertor units, magnetically connecting one upper divertor to one lower divertor two toroidal modules away. A visualization of this geometry is provided in figure 1, where one magnetic island is plotted in blue. The two toroidal modules where the island intersects the divertor targets are plotted in darker color compared to the other toroidal modules. In the front of the image, the island intersects the lower divertor target, plotted in dark gray. The neutral baffles are plotted in green. Each divertor unit consists of a vertical and horizontal target and a set of neutral baffles. The main strike lines are located on the so-called ‘low iota’ portion of the horizontal divertor target and on the vertical target plates. A visualization of the strike lines in relation to the magnetic field is plotted in figure 2.

In figure 2, the red colored areas of the divertor target plates represent the strike line heat flux pattern. Plotted in black is the outline of the last closed flux surface (LCFS) and the magnetic islands, two of which intersect the divertor target plates, at toroidal angle $\varphi = -10°$. The main strike lines are located on the outer separatrix of the magnetic islands, on the side of the islands closest to the pumping gap. The poloidal projection of the parallel heat and particle flux channel is visualized by the dark blue arrows, and is located along this island separatrix [7].

Figure 1. A 3D visualization of the W7-X target geometry. One of the five total islands is plotted in blue. This island intersects the divertor targets in two toroidal modules. These modules are plotted in darker colors as compared to the other toroidal modules. The island intersects the lower target, plotted in dark gray, in the module at the front of the image and the upper divertor in the module in the back of the image. A poloidal slice of the island and the last closed flux surface is plotted in black at toroidal angle $\varphi = -10°$.

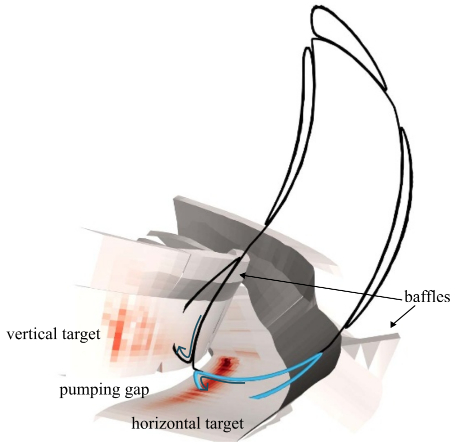

Figure 2. An image of the heat flux onto the divertor target plates as outputted by EMC3-Eirene. The intensity of the red color on the divertor targets (in white) corresponds to the magnitude of the heat flux. The black lines show the outline of the LCFS and the islands. One island intersects the vertical target while the primary strike line occurs on the horizontal target. The island that intersects the horizontal target is outlined in light blue. The dark blue arrows indicate the poloidal projection of the parallel heat flux channel.

2.2. SOL impurity transport

Generally, the transport of impurities through the SOL of magnetic fusion devices is governed by forces parallel and perpendicular to the magnetic field. In steady-state, the following force balance dictates the impurity transport in the parallel direction [3]:

$$0 = m_z \frac{V_{i,\|} - V_{z,\|}}{\tau_s} + \beta_i \frac{\mathrm{d}T_i}{\mathrm{d}s} + \alpha_e \frac{\mathrm{d}T_e}{\mathrm{d}s} + ZeE_\| - \frac{1}{n_z}\frac{\mathrm{d}p_z}{\mathrm{d}s} \tag{1}$$

where $V_{i,\|}$ is the main ion flow velocity parallel to the magnetic field, $V_{z,\|}$ is the impurity flow velocity parallel to the magnetic field, τ_s is the collisional stopping time between the impurity and the main ions, and α_e and β_i are coefficients of the order of Z^2. The first term in equation (1) is the friction force exerted on

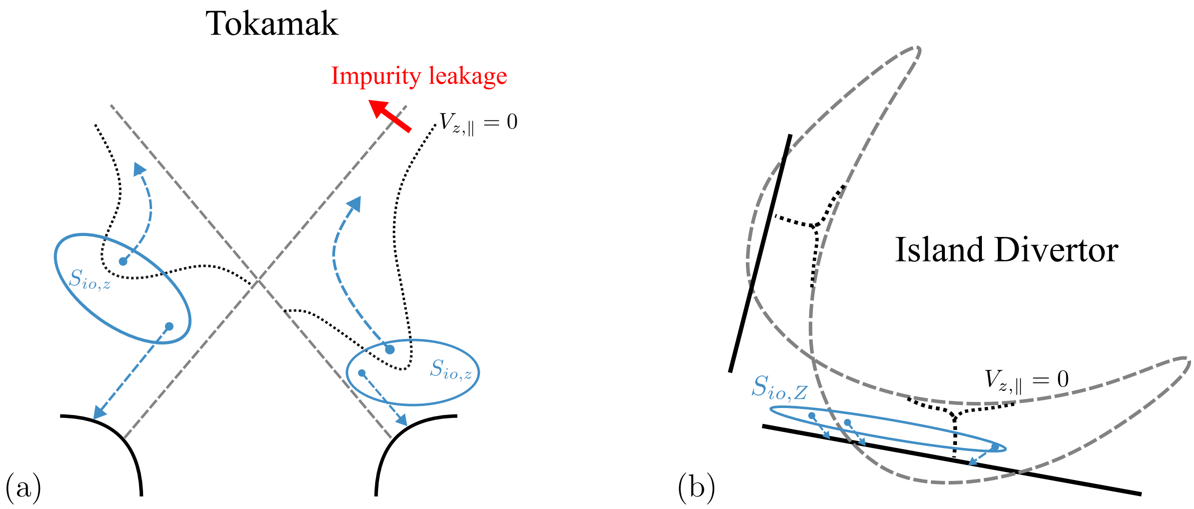

Figure 3. (*a*) A schematic of the poloidal projection of the parallel impurity flow in the tokamak divertor versus (*b*) a schematic of poloidal projection of the parallel impurity flow in the island divertor. The black dotted lines indicate the location of parallel impurity flow stagnation. The solid blue ovals define the region over which the impurity ionization source is located. The dashed arrows indicate the poloidal projection of the parallel impurity flow. Adapted from [11]. © IOP Publishing Ltd All rights reserved.

the impurity from the background ions. Because the parallel main ion flow velocity is generally directed towards the target (downstream), the friction force increases retention. The second term is the ion thermal force on the impurity from the parallel ion temperature gradient. The ion thermal force tends to move impurity particles up the temperature gradient towards the LCFS (upstream). The last term is the parallel impurity pressure gradient force. This term can be split into a parallel ion temperature gradient term (assuming that the impurity ions are thermalized with the main ions $T_z = T_i$) and a parallel impurity density gradient (parallel diffusive) term:

$$\frac{1}{n_z}\frac{\mathrm{d}p_z}{\mathrm{d}s}=\frac{1}{n_z}\frac{\mathrm{d}\left(T_i n_z\right)}{\mathrm{d}s}=\frac{\mathrm{d}T_i}{\mathrm{d}s}-\frac{T_i}{n_z}\frac{\mathrm{d}n_z}{\mathrm{d}s}. \qquad (2)$$

The other terms in equation (1), the electron thermal force and the electric field force, tend to be small in comparison and therefore we will neglect them here. Solving for the parallel impurity flow velocity and using equation (2) results in:

$$V_{z,\parallel}=V_{i,\parallel}+\frac{\tau_s}{m_z}\left[\left(\beta_i-1\right)\frac{dT_i}{\mathrm{d}s}-\frac{T_i}{n_z}\frac{\mathrm{d}n_z}{\mathrm{d}s}\right]. \qquad (3)$$

Equation (3) is valid for both tokamaks and stellarators. For tokamaks, it is well-established that under the majority of cases, the contribution to the parallel impurity flow velocity from the parallel impurity pressure gradient is small [8]. For stellarator island divertors, as will be discussed in more detail later, perpendicular transport of both heat and particles is much more important than in a tokamak [9, 10]. Therefore, the parallel diffusive term in equation (3) can also be ignored for the stellarator case. From the remaining terms, the parallel impurity flow velocity is then determined by the main ion flow velocity with an offset from the ion temperature gradient term. The competition between these two terms determines the location of the parallel impurity flow stagnation point ($V_{z,\parallel}=0$) along the field line.

For tokamaks, recent results have shown that the limit of impurity retention in the SOL is the impurity ionization source beyond the poloidal impurity flow stagnation point (i.e. the sum of the poloidal projection of the parallel impurity flow velocity and the poloidal drift velocity) [8, 11]. In the absence of drifts, the poloidal projection of $V_{z,\parallel}$, determined from equation (3), sets the location of this impurity flow stagnation point. For tokamaks, impurity flow stagnates relatively close to the target, as indicated by the dotted black lines in figure 3(*a*). The ionization source of the impurities, $S_{io,z}$, is indicated by the solid blue ovals. The fraction of impurities which leak to the LCFS is then represented areal overlap of the blue oval with the portion of the SOL located poloidally above the dotted black dashed line. The location of the impurity ionization source, and therefore the amount of impurities which may ionize above the flow stagnation point, is dependent on the impurity ionization energy. Thus, it is typical that impurities high ionization energy (e.g. helium) are less retained than those with low ionization energy (e.g. carbon).

However, due to the small field line pitch (and corresponding long magnetic connection lengths L_c) in the island divertor, perpendicular transport plays a much larger role [9, 10]. This has two effects for the SOL impurity transport. Firstly, it increases the weight of the perpendicular transport of the impurities. Secondly, it significantly reduces the parallel ion temperature gradient. The reduction of the parallel gradient comes from significant binormal heat transport within an island flux tube [10]. A visualization is provided in figure 4, where the LCFS of the island is plotted in gray and a representative field line is plotted as red dots. Each dot represents one full toroidal turn around the machine. From the X-point, the field line still requires approximately 4 toroidal turns to reach the divertor target plate. The approximate binormal direction for the field line below the X-point is visualized in blue. Figure 4 shows that binormal direction is roughly aligned to the radial gradient of T_i, allowing for

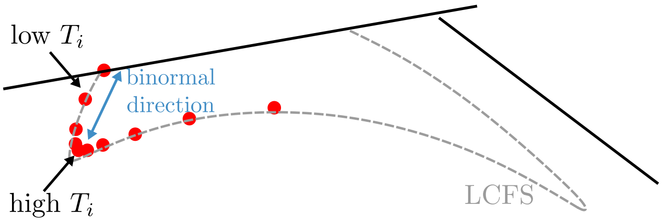

Figure 4. A schematic of the island divertor, with the LCFS plotted as a gray dashed line. A representative field line within the main heat and particle flux-carrying layer is plotted as red dots, with each toroidal turn represented as one dot. The binormal direction is approximately shown in blue.

significant perpendicular transport within the flux tube. This process lowers the upstream ion temperature and flattens the parallel ion temperature gradient [10], significantly reducing the ion thermal force in equation (1). Previous simulation work for the W7-X island SOL has indicated that the friction force dominates over the ion thermal force for the majority of the island SOL, even at very low separatrix density($\sim 1\times10^{19}$ m^{-3} with 10 MW input heating power) [9, 10]. As a result, the parallel impurity flow stagnation point in the parallel heat and particle flux channel is located very far from the target surface, as indicated by the dotted black line in figure 3(*b*). In such a scenario, the impurity ionization source region, indicated by the blue oval, may not overlap with the region of the SOL dominated by the ion thermal force, leading to near perfect retention in the parallel direction.

In the previous experimental campaign, separatrix density levels lower than 1×10^{19} m^{-3} were not reachable due to wall outgassing and limited pumping [12]. Therefore, it is expected that, within the majority of the W7-X operational space, parallel leakage of impurities is small. However, impurities still contaminated the confined plasma. Without impurity seeding, typical Z_{eff} values were between 1.2–1.5 (dominated by carbon) [13, 14]. For neon seeding experiments, Z_{eff} values up to 3 were observed [15]. For the reasons discussed above, impurity transport parallel to the magnetic field is unlikely to be the dominant leakage mechanism. Therefore, it is important to determine where and how the impurities penetrate into the confined plasma under these experimental conditions.

2.3. Simulation set-up

The EMC3-Eirene code [16] is a coupled 3D Monte-Carlo plasma fluid and kinetic neutral model which has shown much success in describing the global behavior observed so far in the W7-X island divertor [15, 17, 18]. The general model is described well elsewhere, and therefore we focus here on the impurity transport model only. The impurities are regarded as ‘trace’ in the sense that their electrons are consisered negligible to the overall particle balance ($n_e = n_i$). However, if desired, one can include the energy lost from impurity line radiation in the electron energy balance. Furthermore, impurities are assumed to always be in thermal equilibrium with the main ions ($T_z = T_i$) and the inertia is neglected in the momentum balance. This assumption is generally a good approximation for the low to medium Z elements used in this work and only becomes more important for heavy impurities, such as tungsten [19]. Impurity neutrals are assumed not to interact with the background plasma ions and therefore follow straight trajectories until their ionization. Parallel to the magnetic field, the steady-state impurity force balance given in equation (1) is used to solve for the parallel impurity flow velcoity $V_{z,\|}$ for each ionization state. The ADAS database is used to calculate the impurity ionization, recombination and power lost due to line radiation [20]. Perpendicular transport is assumed to be anomalous, with anomalous diffusion coefficients specified as an input parameter. No drift effects are included, neither for the main ion nor for the impurities.

The simulations used here utilized the ideal standard magnetic field configuration of W7-X. The standard configuration was the most operated magnetic field configuration in the last experimental phase [21]. The power entering the SOL was set to be 5 MW for the whole device, equally split between electrons and ions. The simulation assumes stellarator symmetry and therefore only one-tenth of the device is modeled. The anomalous particle diffusion coefficient for both main ions and mpurities was set to a constant value of $D = 0.5$ $\mathrm{m}^2\mathrm{s}^{-1}$. The anomalous heat diffusivity for ions and electrons was set to a constant value of $\chi_{e,i} = 3D$. Plasma backgrounds were generated for a separatrix density scan of $n_{e,s} = 1-3\times10^{19}$ m^{-3}, with impurity line radiation coming from intrinsic carbon impurities. Carbon impurities were assumed to sputter chemically ($E_0 = 0.03$ eV) with a 4% yield. The model does not include molecular break-up chains and therefore the carbon neutrals are started as atoms.

All parameters described above are chosen to reproduce W7-X experimentally-relevant conditions, although detailed matching to specific experimental programs were not performed. Previous work has found that this choice of anomalous transport parameters leads to an okay compromise between matching upstream and downstream conditions [22]. Additionally, this choice of input parameters was also capable of reproducing the neutral compression and H-alpha radiation in front of the divertor targets [17]. For the simulations presented in this paper, the radiated power fraction was additionally compared to experiment to ensure that the parameters chosen above led to similar plasma conditions. This comparison is plotted in figure 5. In figure 5, the experimental radiated power fractions from the bolometer diagnostic [13, 23] as a function of the edge density ($\rho \approx 0.98$) from the Thomson scattering diagnostic [24] are plotted as black dots. The experimental dataset is limited to input ECRH heating powers 4.5 MW $<$ $P_{\mathrm{ECRH}} < 5.5$ MW during the boronized phase of the previous experimental campaign (OP1.2b). The total radiated power fraction calculated by EMC3-Eirene for the separatrix density scan described above is plotted as red diamonds. The radiated power fraction in the modeling is the ratio of the total power radiated by impurity line radiation and the total heating power entering the simulation domain, $P_{\mathrm{imp}}/P_{\mathrm{input}}$. There is large scatter in the edge density provided by the Thomson scattering diagnostic due to issues with laser alignment. The

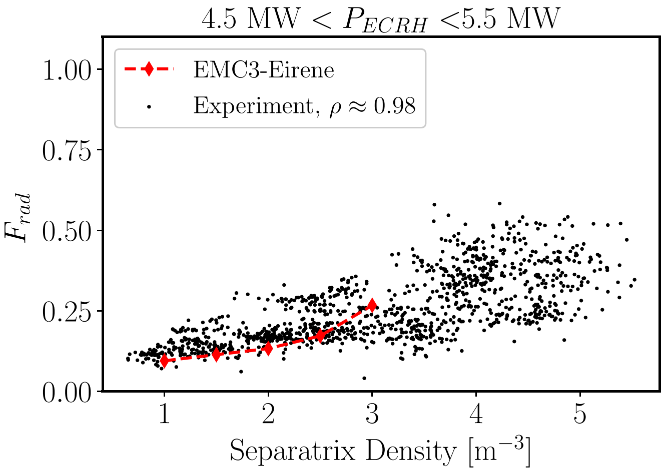

Figure 5. Experimental values of radiated power fraction, F_{rad}, as a function of the edge density value at effective radius $\rho \approx 0.98$ (black dots) compared to EMC3-Eirene (red diamonds).

cause has been found and corrected for the upcoming experimental campaign [25].

Once the plasma backgrounds with intrinsic carbon radiation were converged, different impurities were simulated on the fixed background plasma in full trace approximation (i.e. their line radiation was not included in the overall energy balance) to study their transport and retention properties. These studies comprised scans of impurity species (C, N, Ne, and He) and their initial energy for the simulated background plasma densities. The impurity sources are distributed with the same pattern as the recycling flux of the main ions. The choice to distribute the impurity sources in the same pattern as the recycling flux is to mimic experimental conditions. For carbon, the primary source is erosion on the divertor target plates, with a source rate $\Gamma_{\mathrm{C}} \propto Y_{\mathrm{chem}}\Gamma_{\mathrm{H}}$. For neon and helium, this starting distribution also makes sense: in the OP1.2b operational phase, neon and helium were not pumped. Therefore, a short puff at the beginning of the experimental program was needed to keep a constant impurity content. This means that in steady-state, the information on the initial source location from the puff is lost. Because of this, we assume that the helium and neon impurities are also starting in the same pattern as the recycling flux, since this mimics 'fully recycling' conditions. The only impurity where this assumption may break down is for the nitrogen impurities. In experiment, to maintain a steady-state source of nitrogen the divertor gas injection system [26] must continuously inject nitrogen. However, as will be discussed in section 3, the location of the extrinsic source will likely not play a role in determining whether parallel or perpendicular transport brings the impurities to the LCFS. No recycling and self-sputtering is taken into account. Thus, once an impurity ion hits any surface it will be absorbed. Impurities were launched with an initial energy of 0.03 eV to mimic thermal release from the wall. However, for carbon impurities 2 different energies were investigated (0.03 eV and 10 eV).

3. Results

This section is organized as follows: First a broad overview of the retention capability of the island divertor for each impurities species, as a function of separatrix density, will be shown. This retention capability is quantified by a retention factor f defined as:

$$f = \frac{S_{\mathrm{imp}}\,[A]}{n_{z,\mathrm{LCFS}}\,[m^{-3}]} \tag{4}$$

where S_{imp} is the total impurity source rate in Amps and $n_{z,\mathrm{LCFS}}$ is the total impurity density at the LCFS. The retention factor is defined such that a reduction of the impurity density at the LCFS for a fixed source would increase the retention factor. Thus, for impurities that are sourced in the divertor, this quantifies the global capability of the divertor to keep impurities away from the confined plasma.

Following these global results, we will move towards understanding which transport processes are responsible for the observed global behavior. Three transport processes are investigated. First, we will perform a parallel impurity ion transport analysis to understand if there is any importance of parallel transport in impurity leakage to the LCFS. The parallel transport analysis investigates the relation of the impurity ionization source to the parallel impurity flow stagnation point. Then we will investigate the effects of perpendicular impurity transport. This will be done by scanning the anomalous impurity diffusion coefficient on a fixed plasma background. Finally, we will investigate the role that impurity neutral transport (impurity ionization length) has on determining the impurity retention factor in the W7-X island divertor.

3.1. Global results

The impurity retention factor, defined in equation (4), for each impurity species as a function of main ion separatrix density is plotted in figure 6(*a*). There are several observations that can be made in figure 6(*a*). Firstly, the retention factor changes significantly depending on the impurity species for a given impurity neutral energy. The value of the retention factor follows well the ionization energy of the different impurity species: carbon has the lowest ionization energy and is the most well-retained. Helium has the highest ionization energy and is the least well-retained. The ionization energies are correlated with how far an impurity can travel as a neutral before it ionizes (ionization mean free path). The ionization mean free path (λ_{iz}) can be calculated from the following equation [3]:

$$\lambda_{iz} = \frac{v_0}{n_e \langle \sigma v_{iz} \rangle} \tag{5}$$

where v_0 is the impurity neutral velocity (calculated from its energy) and $\langle \sigma v_{iz} \rangle$ is the impurity ionization rate. The ionization mean free path for the impurities shown in figure 6(*a*) is visualized in figure 6(*b*) for $T_e = 15$ eV and $n_e = 5 \times 10^{19}$ m^{-3}. From figure 6(*b*), the same conclusions can be made

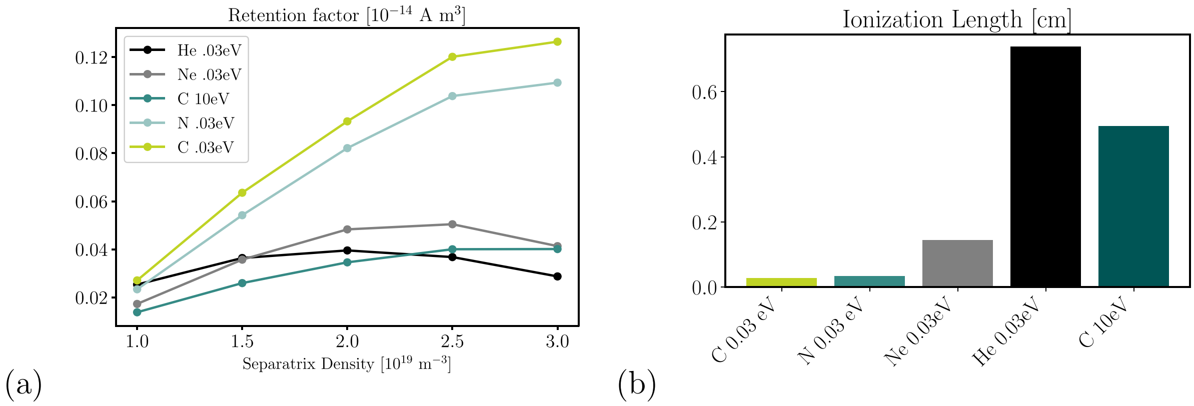

Figure 6. (*a*) The retention factor produced by EMC3-Eirene plotted as a function of separatrix density for the various impurity species. (*b*) An example of the ionization length for each species in (*a*) for $T_e = 15$ eV and $n_e = 5 \times 10^{19}$ m^{-3}.

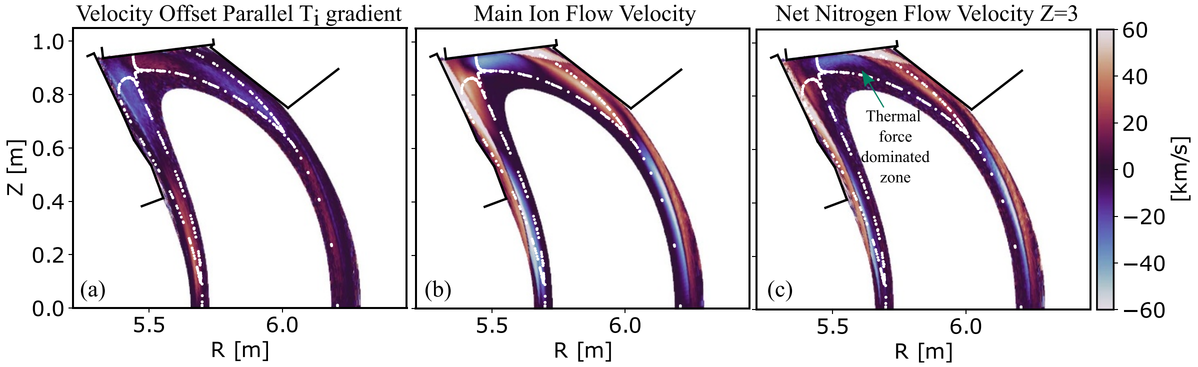

Figure 7. (*a*) The parallel ion temperature gradient contribution and (*b*) the main ion flow velocity contribution to the parallel impurity flow velocity of nitrogen at $n_{e,s} = 1 \times 10^{19}$ m^{-3}. The sum of these two, for the equilibrium nitrogen 3+ flow pattern, is plotted in (*c*). Over the vast majority of the island SOL, the direction of the N^{3+} flow velocity is the same as that of the main ion flow. There exists a small region where the parallel ion temperature gradient term dominates, pointed to by a green line. The magnitude of the flow in this region is very small, leading to the dark color.

about the impurity neutral energy: higher energy carbon neutrals penetrate deeper into the SOL before ionizing, and are therefore less well-retained than low energy impurities of the same species (stated already elsewhere [9]). An explanation of why helium does not follow the typical ionization energy dependence at low separatrix density will be discussed in detail in section 3.5.

Finally, it is clear from figure 6(*a*) that the behavior of the retention factor with density strongly depends on the species. The retention of nitrogen and carbon behave rather similarly, whereas neon and helium see a saturation and then degradation of the retention factor above specific density levels.

We will now investigate the parallel impurity force balance and its relation to the impurity ionization source. This allows us to determine whether impurities ionize in a region of the field line dominated by the ion thermal force. Additionally, it allows us to determine if changes in the amount of impurities ionizing in a thermal force regime is responsible for the density/species behavior plotted in figure 6(*a*).

3.2. *Parallel impurity force balance*

As stated in previous work [10], it is expected that the friction force becomes ever-more dominating over the ion thermal force as the plasma density is increased. Therefore, the parallel impurity force balance is analyzed for the lowest density simulation $n_{e,s} = 1 \times 10^{19}$ m^{-3} as a worst case scenario, both in the simulation set as well as in experiment (as stated in section 2, separatrix densities lower than $n_{e,s} = 1 \times 10^{19}$ m^{-3} were not experimentally attainable in the last operational phase). Equation (3) is used to solve for the equilibrium parallel impurity flow velocity, keeping in mind that the parallel density gradient term is small in comparison to the main ion flow velocity and parallel ion temperature gradient terms:

$$V_{z,\parallel} \approx V_{i,\parallel} + \frac{\tau_s}{m_z}\left[(\beta_i - 1)\frac{\mathrm{d}T_i}{\mathrm{d}s}\right]. \qquad (6)$$

In our simulations, the electric field and electron thermal forces are at least an order of magnitude smaller than the ion thermal and friction forces. The parallel density gradient term is also much smaller than the ion thermal and friction forces except directly near the divertor target plate, where it may be on a similar magnitude as the ion thermal force. However, as will be shown in figure 7, its inclusion will not change the conclusions of this paper: that the friction force is dominant over the majority of the SOL. All terms of equation (6) are plotted for toroidal angle $\varphi = 0°$ in figures 7(*a*)–(*c*). In figure 7(*a*),

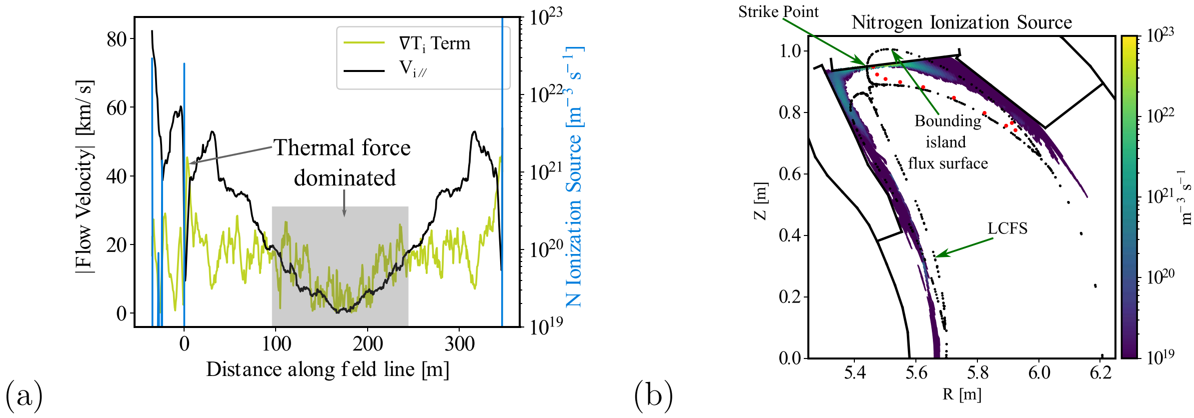

Figure 8. (*a*) A field line profile of the ion temperature gradient contribution to the parallel impurity flow velocity (green), the main ion flow contribution to the parallel impurity flow velocity (black) and the nitrogen ionization source (blue). Thermal force dominated regions of the field line are shaded in gray. The location of the field line is plotted as red dots in (*b*). (*b*) A poloidal cross section of the nitrogen ionization source at toroidal angle 0°. The LCFS and the island separatrix is plotted in black. The strike line is indicated by the intersection of the island separatrix with the target.

the ion temperature gradient contribution to the parallel impurity flow velocity is plotted. Figure 7(*b*) shows the main ion flow contribution to the parallel impurity flow velocity, and figure 7(*c*) shows the equilibrium parallel impurity flow velocity for the N^{3+} ions. (Note: the velocities will be similar for all ionization states because the Z^{-2} dependence in τ_s cancels with the Z^2 dependence in β_i [3].) As is clear from figure 7(*c*), over the vast majority of the island SOL the direction of the parallel nitrogen flow velocity is the same as that of the main ions (figure 7(*b*)). It is only very far upstream, beyond the X-point close to the LCFS, that there exists an area of the SOL where the ion temperature gradient term exceeds that of the main ion flow. The zone is not easily seen in figure 7(*c*) because the magnitude of the velocity is very small. A green arrow is used to indicate the area.

The region where the ion temperature gradient term dominates is easier to see when plotting the magnitude of the two velocity contributions along a field line located within the main heat and particle flux channel, figure 8(*a*). The location of this field line is indicated by the red dots in figure 8(*b*). The field line profile is plotted from target to target, meaning that the midpoint of the profile corresponds to the most-upstream location. The shaded region of figure 8(*a*) indicates the area upstream where the ion temperature gradient contribution (plotted in green) dominates over the main ion velocity contribution (black). The field line profile plotted in figure 8(*a*) indicates an additional area where the ion temperature gradient term dominates. This localized region corresponds to a transition where the field line is less than one full toroidal transit to the target.

However, these areas where the ion temperature gradient term dominates only directly contribute to parallel impurity leakage to the LCFS only if there is a finite impurity ionization source there. The nitrogen ionization source along the field line is plotted in blue in figure 8(*a*). The nitrogen ionization source appears as several very localized peaks along the field line. This strong localization with multiple peaks is a consequence of the modular divertor design in combination with the low field line pitch within the island. As indicated in figure 1, the island rotates poloidally around the LCFS as it moves toroidally around the machine and interacts with multiple divertors (both horizontal and vertical targets). The individual peaks of the nitrogen ionization source correspond to these multiple interactions. The low internal island field line pitch means that it can take more than one toroidal turn before the field line is poloidally far enough away from the target to be outside of the impurity ionization zone. The shape of the nitrogen ionization source in figure 8(*a*) cannot be resolved by the length scale over which the field line is plotted (hundreds of m). In reality, close to the target on the ionization length scale (usually in the cm range), the shape of the ionization source is smooth (figure 8(*b*)). Regardless, figure 8(*a*) indicates that all impurities ionization occurs within regions of the field line where the main ion flow contribution to equation (6) dominates over the ion temperature gradient contribution. Therefore, in the parallel direction and in the absence of perpendicular transport, the impurities are expected to be fully retained in the island divertor. The full poloidal distribution of the nitrogen ionization source (figure 8(*b*)), in comparison to figure 7(*c*), also shows that this statement holds true throughout the entire SOL and not just the chosen field line.

As stated at the beginning of this section, this analysis was performed for the ‘worst case scenario’: where the ion thermal force is largest in magnitude. Even in this case, as outlined above, the impurity ionization source is located entirely in regions of the SOL dominated by the friction force. This indicates that the improvement of impurity retention for nitrogen in the island SOL (figure 6(*a*)) for this density scan cannot arise from variations of the impurity ionization within a region of the SOL dominated by the ion thermal force. It also provides indications that, under these experimentally relevant conditions, impurity leakage to the LCFS is not caused by parallel transport. The only available option left for impurities to

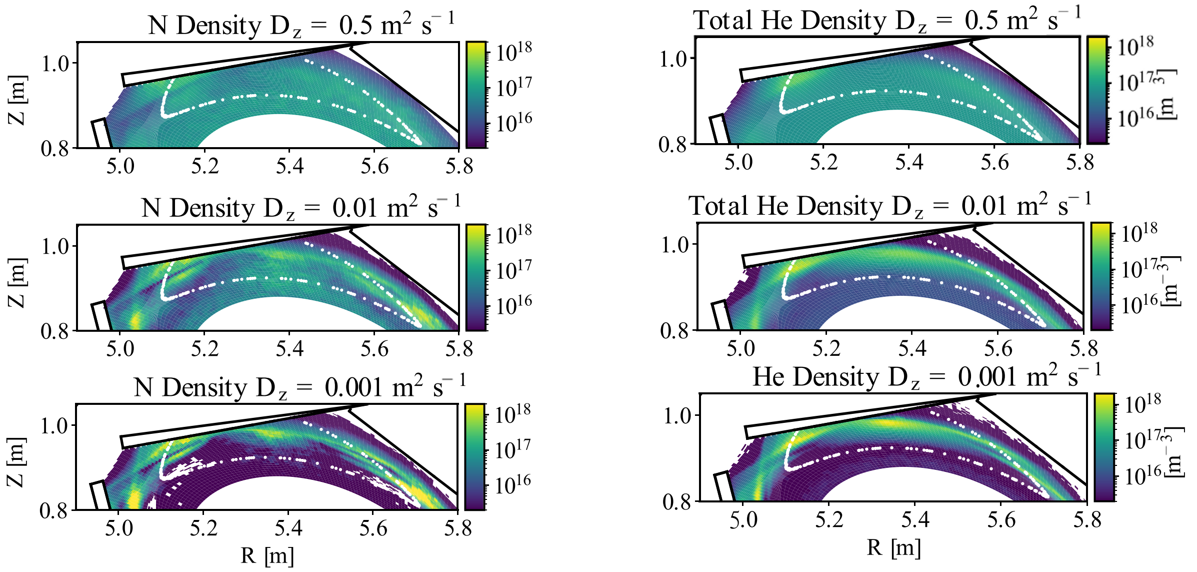

Figure 9. (left) Nitrogen density and (right) Helium density as the impurity anomalous diffusion coefficient is reduced. A strong reduction of impurity density at the LCFS is observed with a decrease of the anomalous diffusion coefficient.

reach the LCFS is via perpendicular transport, which will be discussed next.

3.3. The role of perpendicular transport in impurity leakage

To verify the relevance of perpendicular transport for impurity leakage, the magnitude of the perpendicular transport for the impurities only is reduced in the simulations by scanning the anomalous impurity diffusion coefficient D_z. The plasma background was kept fixed and different trace impurity transport simulations were performed for $D_z = 0.5\ \mathrm{m^2 s^{-1}}$, $D_z = 0.01\ \mathrm{m^2 s^{-1}}$ and $D_z = 0.001\ \mathrm{m^2 s^{-1}}$. The results at $n_{e,s} = 1 \times 10^{19}\ \mathrm{m^{-3}}$ for both nitrogen (left) and helium (right) impurities are plotted in figure 9 at toroidal angle $\varphi = 12^\circ$. For both nitrogen and helium, the distributions plotted in figure 9 represent the sum over all impurity ionization states. The island bounding flux surface is plotted in white.

The reduction of D_z from 0.5 to 0.001 $\mathrm{m^2 s^{-1}}$ leads to a reduction of both nitrogen and helium density at the LCFS by more than an order of magnitude (approximately a factor of 50 for both species). It is a near perfect retention of both the low and high ionization energy species. Figure 9 clearly shows the locations in the island SOL where the impurities accumulate and that the accumulation significantly increases with decreasing D_z. It is noteworthy that the impurities at lower D_z accumulate near the center of the island, where the impurity flow velocity stagnates, $V_{z,\|} \approx 0$ (figure 7(*c*)). This accumulation is consistent with modeling of other devices, such as LHD [27]. The small parallel impurity flow velocity, in combination with the very low internal field line pitch of the island, leads to long impurity residence times near the island center (O-point). These long residence times lead to the local accumulation of impurities even if the impurity source to this location is small. Both the established impurity density gradient as well as the long impurity residence time consequently allows for perpendicular transport across the flow stagnation region to the LCFS.

3.4. The role of ionization mean free path in retention behavior

We have established in the previous sections that impurity leakage in the W7-X island SOL is caused by perpendicular transport. Therefore, the leakage mechanism is fundamentally different from a tokamak. However, as already discussed at the beginning of section 3, the impurity retention factor is influenced by the ionization mean free path (ionization energy/neutral energy) of the impurity species. Longer ionization mean free paths allow neutrals to penetrate deeper into the island SOL before ionizing. *The distance between the ionization location and the LCFS consequently reduces, making it easier for impurity ions to transport perpendicularly across the LCFS. Additionally, the longer ionization mean free path allows more impurity neutrals from the strike line region to ionize close to the impurity flow stagnation region and establish the accumulation there.*

The ionization mean free path directly results in changes to the impurity ionization source distribution. A poloidal and toroidal average of the nitrogen, neon, 10 eV carbon and helium ionization sources is performed to obtain a radial profile of the ionization source for these species. These radial profiles are plotted in figures 10(*a*) and (*b*). Due to the 3D SOL and modular divertor targets, the targets interact with the plasma at different radial locations depending on toroidal angle. The 'target area' labeled in figures 10(*a*) and (*b*) indicates the radial region across which a portion of the poloidal/toroidal area is intersected by target plates. The nomenclature is used to be consistent with other work [18].

There are two mechanisms in which the impurity retention can be reduced/increased:

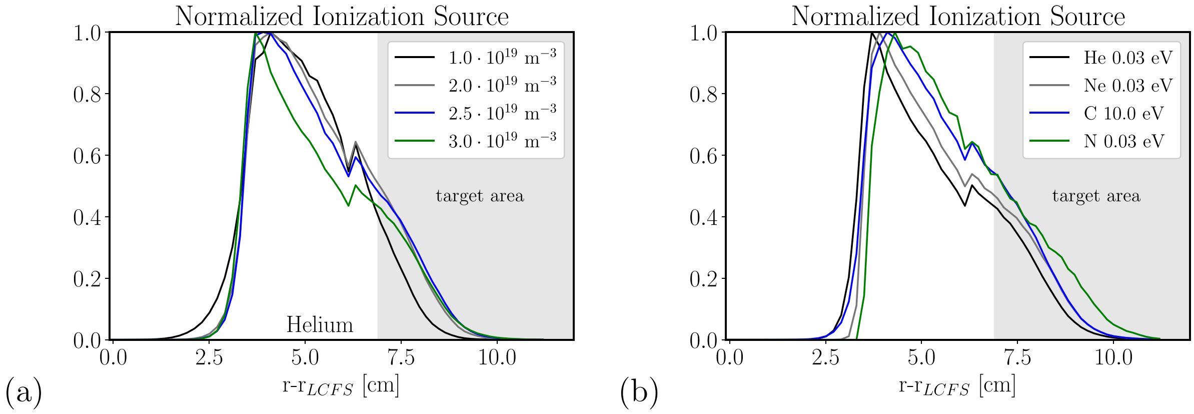

Figure 10. Toroidally and poloidally averaged radial impurity ionization profiles for (*a*) helium as a function of separatrix density and (*b*) for neon, helium, nitrogen and 10 eV carbon at $n_{e,s} = 3.0 \times 10^{19}$ m^{-3}.

(1) The radial profile of the impurity ionization source is shifted towards/away from the LCFS
(2) The radial profile of the impurity ionization source is not shifted, but the profile has become more/less peaked towards the LCFS. An increase in the peakedness of the profile results in a larger fraction of the impurities ionizing further upstream for a fixed ionization front.

Figure 10(*a*) provides an example of the radial profile of the helium ionization source for the separatrix density scan. The differences in the radial profiles of the helium ionization source explains why the helium retention saturates at $n_{e,s} = 2 \times 10^{19}$ m^{-3} and then decreases (figure 6(*a*)). From $n_{e,s} = 1 \times 10^{19}$ m^{-3} to $n_{e,s} = 2 \times 10^{19}$ m^{-3}, the radial ionization profile shifts away from the LCFS. However, from $n_{e,s} = 2 \times 10^{19}$ m^{-3} to $n_{e,s} = 3 \times 10^{19}$ m^{-3}, the radial ionization source profile becomes more peaked towards the LCFS. Although not shown the differences of the radial ionization source profiles of the other impurity species (nitrogen, neon and carbon) as a function of density also explain the density dependence of their retention values plotted in figure 6(*a*).

The differences of the retention between the various impurity species can also be explained by differences in their radial ionization source profiles. An example at $n_{e,s} = 3 \times 10^{19}$ m^{-3} is plotted in figure 10(*b*). The least well-retained impurity at this density level is helium, plotted in black. The most well-retained impurity in the dataset plotted in figure 10(*b*) is nitrogen, plotted in green. As expected, the radial ionization source profile of helium is located closest to the LCFS, while that of nitrogen is located furthest from the LCFS.

3.5. Why helium is more retained than nitrogen at the lowest density

Figure 6(*a*) indicates that helium is better retained in the island SOL than nitrogen at the lowest separatrix density level. This is counter-intuitive when one thinks purely about the ionization mean free path of the impurities. From ionization length arguments alone, the deeper penetration of helium would help it to ionize geometrically closer to the LCFS and flow stagnation region, which would result in a lower retention as compared to nitrogen. This section aims to provide an explanation for what causes this reversal of expectation.

As stated in section 3.3, the dwell time of the impurity in the SOL and in particular the flow stagnation region is important. A longer dwell time leads to higher local impurity densities and higher perpendicular density gradients, which leads to more perpendicular transport and consequently smaller impurity retention of the island SOL. One way to increase the impurity dwell time is to reduce the parallel impurity flow velocity. A reduction of the parallel impurity flow velocity can result from situations where the ion thermal force is not strong enough to cause flow reversal, but is still on a similar magnitude to the friction force. This situation is present in the lowest density simulation case.

Although both nitrogen and helium are in a friction force dominated regime at $n_{e,s} = 1 \times 10^{19}$ m^{3}, the magnitude of the ion thermal force is different for the two impurities. This difference arises mainly due to differences in β_i, but there also exists a difference in τ_s/m_z. Physically, both the ion thermal force and the friction force represent collisional processes. As the transfer of momentum between two colliding species is more efficient between ions of similar mass, it is qualitatively expected that the friction force is increased, and the ion thermal force reduced, for impurities closest in mass to the main ion species (hydrogen). The mass ratio ($\mu = \frac{m_z}{m_i + m_z}$) appears in the following way for β_i [3]:

$$\beta_i = \frac{3\left(\mu + 5\sqrt{2}Z^2\left(1.1\mu^{5/2} - 0.35\mu^{3/2}\right) - 1\right)}{2.6 - \mu + 5.4\mu^2} \quad (7)$$

and for τ_s/m_z:

$$\frac{\tau_s}{m_z} \propto \frac{m_z/\sqrt{m_i}}{Z^2\left(m_z + m_i\right)}. \quad (8)$$

Computing these factors, it is found that $\beta_{i,\mathrm{He}} \approx 1.8Z^2$, $\tau_{s,\mathrm{He}}/m_{\mathrm{He}} \propto 0.8Z^{-2}$, $\beta_{i,\mathrm{N}} \approx 2.4Z^2$, $\tau_{s,\mathrm{N}}/m_{\mathrm{N}} \propto 0.93Z^{-2}$. Multiplying these factors together we find that $\beta_{i,\mathrm{He}}\tau_{s,\mathrm{He}}/m_{\mathrm{He}} \equiv f_{\mathrm{He}} \approx 1.44$ while $\beta_{i,\mathrm{N}}\tau_{s,\mathrm{N}}/m_{\mathrm{N}} \equiv f_{\mathrm{N}} \approx 2.24$. Taking the ratio $f_{\mathrm{N}}/f_{\mathrm{He}}$ indicates that, in this simplified picture, the impact of the ion thermal force is about 1.5 times stronger

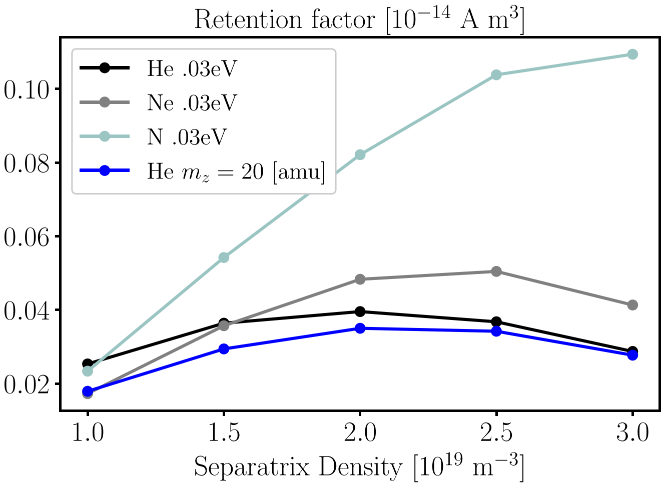

Figure 11. The retention factor, equation (4), including helium simulations where the mass of helium was set to be 20 amu in β_i and τ_s/m_z.

for nitrogen than for helium. These differences are much smaller among the other impurities in the dataset, because μ does not vary significantly from carbon ($\mu = 0.92$) to neon ($\mu = 0.95$).

Therefore, the ion thermal force is smaller for helium ($\mu = 0.8$) than for the other impurities. Consequently, the magnitude of its parallel flow velocity (which is directed towards the target plate), (equation (6)) is larger at low density compared to the other impurity species. Thus, its dwell time in the SOL is smaller. In the simulation, it is possible to prove directly that it is the similarity of the helium mass to the hydrogen mass which causes the deviation of the retention factor from the typical ionization length scaling at low density. The impurity mass in τ_s and β_i is artificially set to be the mass of a heavier impurity (in this case 20 amu) and the trace impurity transport simulation is re-run for helium. The mass of helium is only modified in these two terms and is kept to 4 amu for the rest of the transport calculation. The modified retention behavior with density is consistent with the naive expectations as shown in figure 11.

The helium from the previous simulation set with physically correct mass, plotted in black, is compared to the case where the mass of helium in the τ_s and β_i terms are modified, plotted in blue. The differences between the two cases are largest for the lowest 2 separatrix densities. As the density increases, the retention differences between the ‘normal’ helium case and the 1heavy’ helium case become small. Eventually, they equal each other at the highest separatrix density simulation. Furthermore, the 1heavy’ helium simulation set shows helium as the worst-retained impurity over the entire density range. These results indicate that it is indeed the small mass of helium that leads to the deviation of the retention factor from the typical ionization length scaling. The mass of deuterium and tritium comes even closer to that of helium, implying that the retention of helium would be further improved in DT plasmas.

4. Discussion and conclusion

The EMC3-Eirene results presented above have shown:

(1) All impurity ionization takes place in a region of the island SOL dominated by the friction force. As a result, *parallel transport does not directly contribute to impurity leakage in W7-X.*
(2) Perpendicular transport, in particular through the island O-point region, is responsible for impurity leakage in the standard magnetic field configuration. Suppressing perpendicular transport leads to a near perfect retention of impurities in the island SOL in the simulated low F_{rad} conditions.
(3) The impurity retention factor is different depending on the plasma background or the impurity species. These differences can be attributed to changes in the ionization mean free path of the impurities. However, *unlike a tokamak*, the retention differences from ionization mean free path are related to the perpendicular distance between the impurity ionization location and the LCFS, not changes in the amount of impurities ionized in a region of the SOL dominated by the ion thermal force.
(4) In cases where the ion thermal force significantly reduces the magnitude of the parallel impurity flow velocity, but impurity flow is still directed towards the target, the impurity retention is reduced. This is attributed to an increase of the impurity dwell time in the SOL. However, it is important to note that this decrease of impurity retention still arises from perpendicular transport: the longer dwell time allows for more particles to diffuse to the LCFS. Due to the dependence of the ion thermal force (β_i) on the impurity mass, the increase in impurity dwell time is smaller for helium than for other impurities.

These conclusions are drawn from results taken from EMC3-Eirene modeling of experimentally achievable plasma conditions. The lack of parallel forces bringing impurities to the LCFS may prove to be a beneficial feature of island divertor transport in comparison to that of a tokamak. As an example, we compare the impurity enrichment level of nitrogen in these simulations as compared to that of a single null tokamak divertor. To do this, we compute the downstream pressure-weighted average of the nitrogen concentration and compare to the nitrogen concentration at the separatrix. The downstream pressure-weighted average is used because it largely reflects the location of the plasma strike line. In our simulation at $n_{e,s} = 2.5 \times 10^{19}$ m^{-3}, we find that the nitrogen enrichment level $\eta_{\mathrm{N}} = c_{\mathrm{N,div}}/c_{\mathrm{N,sep}} = 10.8$. Levels at similar input power, separatrix density, and trace nitrogen for SOLPS-ITER simulations of ASDEX-U (without drifts included) show $\eta_{\mathrm{N}} \approx 1.5$ in the outer divertor [28]. Experimental levels of nitrogen enrichment at ASDEX-U range between 2–5 [29, 30]. However, it is important to note that drifts have an impact on the level of enrichment in tokamaks, generally being unfavorable for impurity retention [11]. Therefore, the enrichment value for nitrogen in W7-X using EMC3-Eirene without drifts should be taken as an upper bound rather than as a determined value.

The importance of perpendicular transport on the impurity contamination in the island was tested by significantly reducing the anomalous impurity diffusion coefficient D_z and recalculating the impurity transport on the fixed plasma background. When reducing D_z from 0.5 to 0.001 $\mathrm{m^2 s^{-1}}$, both nitrogen and helium impurities saw a similar, significant reduction (approximately a factor of 50) of total density at the LCFS, indicating the perpendicular transport is indeed setting the density at the LCFS in these experimentally relevant plasma scenarios. The strength of impurity retention is directly related to the distance between the impurity ionization location and the LCFS.

Simulations also provided the interesting result that, in regions where the thermal force is not dominant, but significant enough to offset the impurity flow velocity, helium is better retained than other impurities, even though the ionization length of helium is in some cases much longer. This results from the mass of helium being comparable to hydrogen and hence, a larger change of the reduced mass that sets the ion thermal force. The ion thermal force should be even more reduced for helium in comparison to other species in deuterium plasmas, where the difference in mass between helium and the main species becomes even smaller.

The largest uncertainty in the results presented in this work is the effect of drifts on the main ion and impurity flows. Quantification of drift effects are still in the preliminary phase in W7-X, with most effort concentrated on the poloidal $\vec{E}_r \times \vec{B}$ flow [31, 32]. Depending on the direction of the magnetic field, this drift flow poloidally shifts the location of maximum pressure along the outer separatrix of the island, from the geometrical midpoint of the island to somewhere in between this midpoint and the X-point [32]. This effect would poloidally shift the main ion flow stagnation region closer to the strike line on the upper divertor target plates and away from the strike line on the lower divertor target plates, or vice versa upon reversal of the magnetic field direction. Although one can expect a redistribution of heat and particles from the drift effects, the poloidal drift is essentially a binormal transport mechanism. As discussed in section 2, binormal transport has the effect of reducing the parallel ion temperature gradient. Therefore, the inclusion of the drift will likely not increase the magnitude of the ion thermal force, and the parallel impurity ion flow should still be well-coupled to the main ion flow. Nonetheless, the inclusion of the poloidal drift velocity for the impurities would decrease the dwell time in the parallel flow stagnation region, counteracting the perpendicular transport mechanism that has been described in section 3.3. At the same time, unless drifts are completely dominating the particle dynamics, there should be a location within the island where the poloidal component of the parallel impurity flow velocity exactly cancels with the poloidal impurity drift flow velocity. This would lead to a 'net zero' poloidal flow stagnation region where the perpendicular transport mechanism we have discussed would still play a role.

Experimentally, the relevant operational density regime for W7-X is close to detachment, which occurs at separatrix densities above 3×10^{19} [14, 18, 33]. At such density levels, the ion thermal force is so small that it does not even offset any of the impurity species' flow from the main ion flow [9]. In a simulation at 3×10^{19} $\mathrm{m^{-3}}$ where the ion thermal force was removed and was compared to a simulation which was identical, except for including the ion thermal force showed a minimal difference of total impurity density at the LCFS ($\sim$10%). On top of this, it is known that the upstream temperature reduces upon the onset of detachment [18], which is further expected to reduce the parallel temperature gradients and thus the ion thermal force. Therefore, it is expected that the retention follows the expected ionization length scaling in the relevant operational space. The differences in impurity flow resulting from ion thermal force differences between helium and nitrogen at very low density may be accessible in the next experimental campaign using the coherence imaging spectroscopy diagnostic [34–36]. Though not reactor-relevant, these measurements would be interesting for validation of the simulation results presented here.

Acknowledgments

This work as been carried out within the framework of the EUROfusion Consortium, funded by the European Union via the Euratom Research and Training Programme (Grant Agreement No 101052200 - EUROfusion). Views and opinions expressed are however those of the author(s) only and do no necessarily reflect those of the European Union or the European Commission. Neither the European Union nor the European Commission can be held responsible for them.

ORCID iDs

V.R. Winters https://orcid.org/0000-0001-8108-7774
F. Reimold https://orcid.org/0000-0003-4251-7924
Y. Feng https://orcid.org/0000-0002-3846-4279
V. Perseo https://orcid.org/0000-0001-8473-9002
M. Beurskens https://orcid.org/0000-0002-3354-0279
S. Bozhenkov https://orcid.org/0000-0003-4289-3532
K.J. Brunner https://orcid.org/0000-0002-0974-0457
G. Fuchert https://orcid.org/0000-0002-6640-2139
R. Koenig https://orcid.org/0000-0002-4772-0051
J. Knauer https://orcid.org/0000-0001-7359-6472
E. Scott https://orcid.org/0000-0002-1389-1151
D. Zhang https://orcid.org/0000-0002-5800-4907

References

[1] Bosch H.S. *et al* 1997 *Plasma Phys. Control. Fusion* **39** 1771
[2] Goetz J.A., Lipschultz B., Pitcher C.S., Terry J.L., Bonoli P.T., Rice J.E. and Wukitch S.J. 1999 *J. Nucl. Mater.* **266–269** 354–9
[3] Stangeby P.C. 2000 *The Plasma Boundary of Magnetic Fusion Devices* (IOP Publishing Ltd)
[4] Feng Y. *et al* 2014 *Contrib. Plasma Phys.* **54** 426–31

[5] Geiger J., Beidler C.D., Feng Y., Maaßberg H., Marushchenko N.B. and Turkin Y. 2015 *Plasma Phys. Control. Fusion* **57** 014004
[6] Sunn Pedersen T. *et al* 2018 *Plasma Phys. Control. Fusion* **61** 014035
[7] König R. *et al* 2002 *Plasma Phys. Control. Fusion* **44** 2365
[8] Stangeby P.C. and Moulton D. 2020 *Nucl. Fusion* **60** 106005
[9] Feng Y. *et al* 2009 *Nucl. Fusion* **49** 095002
[10] Feng Y., Kobayashi M., Lunt T. and Reiter D. 2011 *Plasma Phys. Control. Fusion* **53** 024009
[11] Senichenkov I.Y., Kaveeva E.G., Sytova E.A., Rozhansky V.A., Voskoboynikov S.P., Veselova I.Y., Coster D.P., Bonnin X. and Reimold F. 2019 *Plasma Phys. Control. Fusion* **61** 045013
[12] Schlisio G. *et al* 2021 *Nucl. Fusion* **61** 036031
[13] Zhang D. *et al* 2021 *Nucl. Fusion* **61** 126002
[14] Jakubowski M. *et al* 2021 *Nucl. Fusion* **61** 106003
[15] Effenberg F. *et al* 2019 *Nucl. Fusion* **59** 106020
[16] Feng Y., Sardei F. and Kisslinger J. 1999 *J. Nucl. Mater.* **266–269** 812–8
[17] Winters V.R. *et al* 2021 *Plasma Phys. Control. Fusion* **63** 045016
[18] Feng Y. *et al* 2021 *Nucl. Fusion* **61** 086012
[19] Schmid K. and Lunt T. 2018 *Nucl. Mater. Energy* **17** 200–5
[20] Summers H.P. 2004 The ADAS user manual (version 2.6) (available at: www.adas.ac.uk)
[21] Sereda S. *et al* 2020 *Nucl. Fusion* **60** 086007
[22] Feng Y. *et al* 2021 *Nucl. Fusion* **61** 106018
[23] Zhang D. *et al* 2010 *Rev. Sci. Instrum.* **81** 10E134
[24] Pasch E., Beurskens M.N.A., Bozhenkov S.A., Fuchert G., Knauer J. and Wolf R.C. 2016 *Rev. Sci. Instrum.* **87** 11E729
[25] Fuchert G., Nelde P., Pasch E., Beurskens M.N.A., Bozhenkov S.A., Brunner K.J., Meineke J., Scott E.R. and Wolf R.C. 2022 *J. Intsrum.* **17** C03012
[26] Barbui T., Gallop B., Liu J., Miyagawa P.S., Phillips P.W., Pownall G.D., Robinson D. and Weidberg A.R. 2019 *J. Intsrum.* **14** C07014
[27] Dai S., Kobayashi M., Kawamura G., Morita S., Zhang H.M., Oishi T., Feng Y., Wang D.Z. and Suzuki Y. 2016 *Nucl. Fusion* **56** 066005
[28] Hitzler F., Wischmeier M., Reimold F. and Coster D.P. 2020 *Plasma Phys. Control. Fusion* **62** 085013
[29] Kallenbach A. *et al* 2017 *Nucl. Fusion* **57** 102015
[30] Henderson S.S. *et al* 2020 Experimental impurity concentrations required to reach detachment on aug and jet *28th IAEA Fusion Energy Conf.* (*FEC 2020*) (*Virtual, 10–15 May 2021*) (available at: https://nucleus.iaea.org/sites/fusionportal/Shared%20Documents/FEC%202020/fec2020-preprints/preprint0923.pdf)
[31] Hammond K.C. *et al* 2019 *Plasma Phys. Control. Fusion* **61** 125001
[32] Kriete D.M. *et al* 2023 *Nucl. Fusion* **63** 026022
[33] Schmitz O. *et al* 2021 *Nucl. Fusion* **61** 016026
[34] Perseo V., Gradic D., König R., Ford O.P., Killer C., Grulke O. and Ennis D.A. 2020 *Rev. Sci. Instrum.* **91** 013501
[35] Perseo V. *et al* 2021 *Nucl. Fusion* **61** 116039
[36] Perseo V., Effenberg F., Gradic D., König R., Ford O.P., Reimold F., Ennis D.A., Schmitz O. and Sunn Pedersen T. 2019 *Nucl. Fusion* **59** 124003